Modeling MESSENGER observations of calcium in Mercury's exosphere

Matthew H. Burger,[1,2] Rosemary M. Killen,[1] William E. McClintock,[3] Ronald J. Vervack Jr.,[4] Aimee W. Merkel,[3] Ann L. Sprague,[5] and Menelaos Sarantos[6,7]

Received 8 June 2012; revised 19 October 2012; accepted 22 October 2012; published 7 December 2012.

[1] The Mercury Atmospheric and Surface Composition Spectrometer (MASCS) on the MESSENGER spacecraft has made the first high-spatial-resolution observations of exospheric calcium at Mercury. We use a Monte Carlo model of the exosphere to track the trajectories of calcium atoms ejected from the surface until they are photoionized, escape from the system, or stick to the surface. This model permits an exploration of exospheric source processes and interactions among neutral atoms, solar radiation, and the planetary surface. The MASCS data have suggested that a persistent, high-energy source of calcium that was enhanced in the dawn, equatorial region of Mercury was active during MESSENGER's three flybys of Mercury and during the first seven orbits for which MASCS obtained data. The total Ca source rate from the surface varied between 1.2×10^{23} and 2.6×10^{23} Ca atoms s^{-1}, if its temperature was 50,000 K. The origin of this high-energy, asymmetric source is unknown, although from this limited data set it does not appear to be consistent with micrometeoroid impact vaporization, ion sputtering, electron-stimulated desorption, or vaporization at dawn of material trapped on the cold nightside.

Citation: Burger, M. H., R. M. Killen, W. E. McClintock, R. J. Vervack Jr., A. W. Merkel, A. L. Sprague, and M. Sarantos (2012), Modeling MESSENGER observations of calcium in Mercury's exosphere, *J. Geophys. Res.*, *117*, E00L11, doi:10.1029/2012JE004158.

1. Introduction

[2] Mercury possesses a tenuous atmosphere that is collisionless down to the planetary surface, i.e., a surface-bounded exosphere. The atmosphere was discovered by the Mariner 10 airglow spectrometer, which recorded emission from hydrogen, helium, and possibly oxygen [*Broadfoot et al.*, 1974, 1976]. Ground-based observers have discovered a number of additional species, including Na [*Potter and Morgan*, 1985], K [*Potter and Morgan*, 1986], Ca [*Bida et al.*, 2000], and Al and Fe (which were given strict upper limits by *Bida and Killen* [2011]). The MErcury Surface, Space ENvironment, GEochemistry, and Ranging (MESSENGER) spacecraft instrument payload includes the Mercury Atmospheric and Surface Composition Spectrometer (MASCS) [*McClintock and Lankton*, 2007], the Ultraviolet and Visible Spectrometer (UVVS) channel of which successfully detected Mg in Mercury's exosphere during two of MESSENGER's three flybys of Mercury [*McClintock et al.*, 2009; *Vervack et al.*, 2010]. MASCS observations during the orbital phase of the MESSENGER mission, which began in March 2011, have confirmed the presence of O, although at a much lower intensity than the Mariner 10 upper limit [*Vervack et al.*, 2011].

[3] Whereas the Na component of Mercury's exosphere has been regularly observed from the ground for more than 25 years, Ca detections are more sparse as the Ca emission is fainter than that of Na and at a wavelength difficult to observe from the ground. *Bida et al.* [2000] reported detections of Ca emission above Mercury's poles. From the line widths, they estimated a temperature $\gtrsim$12,000 K. This energetic Ca was hypothesized to result from ion sputtering in regions of the surface open to precipitating solar wind ions, as had been suggested for the origin of high-latitude enhancements in Na emission [*McGrath et al.*, 1986].

[4] *Killen et al.* [2005] reported results from 22 nights of Ca observations from the Keck Observatory between 1997

[1]Planetary Magnetospheres Laboratory, Solar System Exploration Division, NASA Goddard Space Flight Center, Greenbelt, Maryland, USA.
[2]Goddard Earth Sciences Technology and Research, Morgan State University, Baltimore, Maryland, USA.
[3]Laboratory for Atmospheric and Space Physics, University of Colorado Boulder, Boulder, Colorado, USA.
[4]The Johns Hopkins University Applied Physics Laboratory, Laurel, Maryland, USA.
[5]Lunar and Planetary Laboratory, University of Arizona, Tucson, Arizona, USA.
[6]Heliophysics Science Division, NASA Goddard Space Flight Center, Greenbelt, Maryland, USA.
[7]Goddard Planetary Heliophysics Institute, University of Maryland, Baltimore County, Catonsville, Maryland, USA.

Corresponding author: M. H. Burger, Planetary Magnetospheres Laboratory, Solar System Exploration Division, NASA Goddard Space Flight Center, 8800 Greenbelt Rd., Greenbelt, MD 20771, USA. (matthew.burger@nasa.gov)

0148-0227/12/2012JE004158

Table 1. MESSENGER Trajectory Parameters[a]

Orbit Number	C/A (UTC)	TAA (deg)	r (AU)	dr/dt (km/s)	τ (h)	g (phot/s)	$\lambda_\odot$ (deg)	$d\lambda_\odot/dt$ (deg/day)
M1	2008 Jan 14 19:04	285	0.35	−9.7	0.49	22.2	185	−1.3
M2	2008 Oct 6 08:40	293	0.34	−9.2	0.47	22.8	3	−1.0
M3	2009 Sep 29 21:55	331	0.31	−4.9	0.39	16.9	0	−0.1
22	2011 Mar 29 02:24	74	0.35	9.7	0.49	21.9	356	−1.3
23	2011 Mar 29 14:28	76	0.35	9.8	0.50	21.8	355	−1.3
24	2011 Mar 30 02:33	79	0.36	9.9	0.50	21.6	354	−1.4
25	2011 Mar 30 14:37	81	0.36	9.9	0.51	21.4	354	−1.5
26	2011 Mar 31 02:41	83	0.36	10.0	0.52	21.2	353	−1.6
27	2011 Mar 31 14:46	86	0.37	10.0	0.53	20.9	352	−1.6
28	2011 Apr 01 02:50	88	0.37	10.1	0.54	20.6	351	−1.7

[a]MESSENGER's flybys of Mercury are prefixed with "M". C/A = time of MESSENGER closest approach to Mercury (time of periapsis during the orbital mission), TAA = true anomaly angle, r = Mercury's distance from the Sun, dr/dt = Mercury's radial velocity relative to the Sun, τ = photoionization lifetime, g = g-value from *Killen et al.* [2009], $\lambda_\odot$ = subsolar longitude in IAU planet-fixed coordinate system, and $d\lambda_\odot/dt$ = rate of change of the subsolar longitude. Owing to a spacecraft "safe hold" before the M3 closest approach, no data were obtained after 21:48 UTC during that encounter.

and 2002. A general increase in Ca radiance was seen between 1997, when no emission was detected, through 2000. This increase was attributed to increases in the g-values, the product of the photon flux at the Ca resonant transition wavelength (422.7 nm in the rest frame of a Ca atom) and the scattering efficiency per atom, with the column density varying only by a factor of ∼2 between 1998 and 2000. These observations confirmed the presence of an energetic Ca source. *Killen et al.* [2005] concluded that the likely source of exospheric Ca was either ion sputtering or dissociation of molecular calcium (possibly in the form of CaO or CaS) launched from the surface in micrometeoroid impact vapor. Photodissociation of CaO by Lyman-α imparts ∼2 eV kinetic energy (equivalent to ∼3 km s^{-1}) to the resulting Ca neutral, sufficient to explain the hot component of the Ca exosphere that has been observed. If CaO is the source, this formation mechanism also predicts the existence of an escaping oxygen component to Mercury's exosphere.

[5] Before orbit insertion, MESSENGER made three flybys of Mercury during which high-spatial-resolution observations of emission from neutral species and ions in Mercury's exosphere were completed by UVVS [*McClintock et al.*, 2008, 2009; *Vervack et al.*, 2010]. These observations revealed the presence of two previously unobserved species, Mg and Ca^+, and yielded high-spatial-resolution maps of Na, Ca, Ca^+, and Mg in the tail extending over the nightside of the planet and over Mercury's poles (Ca^+ was detected in a narrow region ∼2–3 Mercury radii anti-sunward of Mercury). From orbit, UVVS observations of the three neutrals Na, Ca, and Mg have been made almost daily, and searches have been conducted for other neutral and ionic species, both known (e.g., K, Al, Fe, Ca^+) and expected (e.g., O, S, Mg^+) to be present.

[6] A puzzling feature of the neutral observations is that Na, Ca, and Mg exhibit distinct spatial distributions that cannot be explained by differences in photoionization lifetimes or the effects of solar radiation pressure. The implication is that these three species have distinct source mechanisms and/or are ejected from distinct regions on the surface. *Burger et al.* [2010] applied the results of *Killen et al.* [2004] to demonstrate that low-energy photon-stimulated desorption (PSD) – the desorption of atoms from the surface by ultraviolet (UV) photons – was the primary source of the escaping sodium population during the first two flybys. In contrast, the observed calcium and magnesium were ejected with velocities indicative of high-temperature sources (>10,000 K) [*Vervack et al.*, 2010; *Killen et al.*, 2010], consistent with the ground-based observations of Ca [*Bida et al.*, 2000; *Killen et al.*, 2005]. However, *Sarantos et al.* [2011] determined that at least two source temperatures were needed to explain the MESSENGER Mg observations. A high-energy source was required to explain the data far from Mercury, whereas observations close to the planet indicated a reservoir of volatile Mg acted upon by lower-energy source processes.

[7] In this study, we present model simulations of the Ca emission observed by UVVS during the three flybys and seven early MESSENGER orbits. We present an empirical description of the spatial and energy distributions of the likely Ca source. Description of the physical mechanism responsible for this source must await a better understanding of how the source region varies with time, surface geology, and magnetospheric and solar wind interactions with Mercury's surface. The organization of this paper is as follows. In Section 2 we describe the UVVS observations obtained during the MESSENGER Mercury flybys. In Section 3, we describe the Monte Carlo model, possible Ca source and loss processes, and how these processes are implemented in the model. Model simulations of the flyby data are shown in Section 4 to characterize the Ca source. In Section 5, we apply these results to the data obtained by UVVS during the first four days of orbital science operations. Section 6 presents a summary of our results and a discussion of possible physical mechanisms that can explain the dawn source of atomic calcium.

2. UVVS Observations of Calcium

[8] MESSENGER executed three flybys of Mercury before entering orbit on 18 March 2011. Important parameters related to these flybys are given in Table 1, including Mercury's true anomaly angle (TAA), heliocentric distance, and heliocentric radial velocity. Further details regarding these data and the observational geometries beyond those presented below have been given by *McClintock et al.* [2008, 2009] and *Vervack et al.* [2010].

[9] The flyby data have been divided into sub-groups on the basis of the particular flyby and the observational strategy. Tail observations were made during all three flybys in the region anti-sunward of Mercury during MESSENGER's

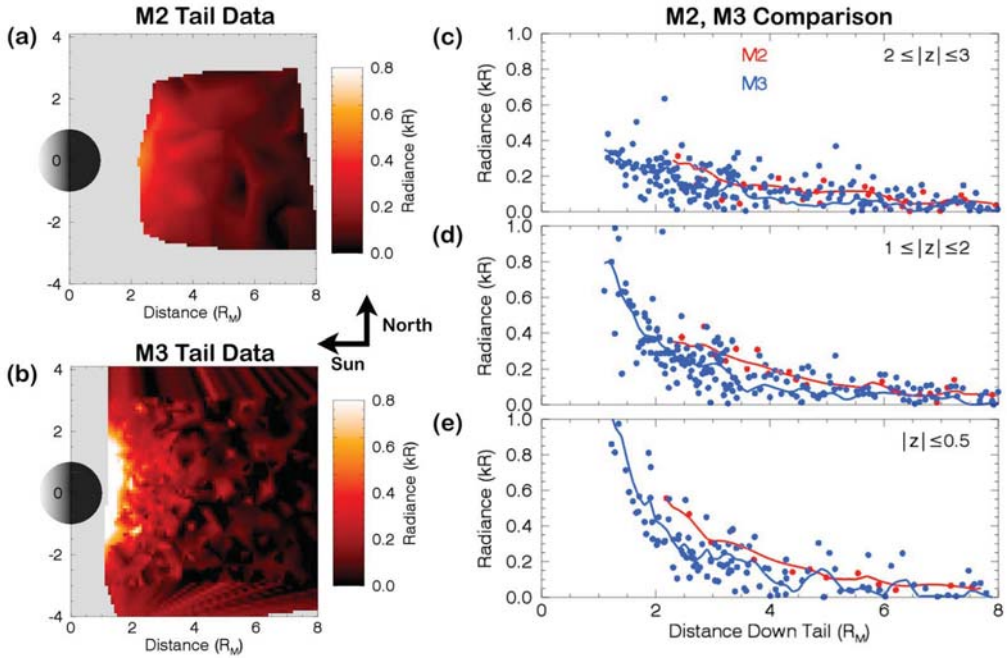

Figure 1. Comparison between tail data from M2 and M3. (a) Constructed image from M2 (see text for details). (b) Constructed image from M3 with the same color scale as in Figure 1a. (c) Comparison of M2 and M3 tail data for which the UVVS line of sight crossed the noon–midnight plane between 2 and 3 R_M from the equatorial plane. The individual data points are shown by filled red and blue circles for M2 and M3, respectively. The solid lines give the mean values within bins of width 0.1 R_M along the tail. (d) Comparison of M2 and M3 tail data for which the UVVS line of sight crossed the noon–midnight plane between 1 and 2 R_M from the equatorial plane. (e) Comparison of M2 and M3 tail data for which the UVVS line of sight crossed the noon–midnight plane within 0.5 R_M of the equatorial plane.

approach toward the planet. Calcium was observed in the tail during the second and third flybys, designated M2 and M3, respectively (Figure 1). Images have been constructed from the observations using the method of *McClintock et al.* [2008]. UVVS does not make two-dimensional observations of the calcium tail; instead, it captures the emission along successive lines of sight in a $1^\circ \times 0.04^\circ$ slit. The spacecraft location and the direction of the line of sight change between observations.

[10] Images of the flyby observations, presented in Figures 1a and 1b, were constructed by mapping each radiance measurement to the point where the UVVS line of sight crossed the noon–midnight plane – the x–z plane in the Mercury solar orbital (MSO) coordinate system, in which x points sunward, z is perpendicular to Mercury's orbital plane and is positive northward, and y completes the right-handed system – and interpolating the irregularly scattered points onto a regular grid. The spacecraft rocked along its noon–midnight axis to map the tail in the north–south plane; the changing angle of the line of sight relative to the equatorial plane is not represented in the projected image. Figures 1c to 1e compare the tail observations from M2 and M3 using the method of *Burger et al.* [2010]. In Figure 1c, we show the radiances from all measurements for which the UVVS line of sight intersected the noon–midnight plane between 2 R_M and 3 R_M from the equatorial ($z = 0$) plane (hereafter, the "upper region"), where R_M is Mercury's radius or 2440 km. The solid lines give the average radiance in 0.1 R_M bins along the tail. Figure 1d shows the points for which the lines of sight intersect between 1 and 2 R_M from the equatorial plane (the "mid region"); in Figure 1e, only those points falling within 0.5 R_M of the equatorial plane (the "central region") are shown. There is no evidence of a north–south asymmetry in either the M2 or M3 tail data (auxiliary material Figures S1 and S2).[1]

[11] The Ca emission in the tail at 422.7 nm may have been brighter during M2 than M3, although the scatter in the data is large. At 4 R_M anti-sunward of Mercury, the Ca intensity ratio $R = I_{M2}/I_{M3}$ was 1.8 ± 1.6 for observations in the upper region, 1.9 ± 1.0 for those in the mid region, and 2.0 ± 1.4 for those in the central region. Looking at all the tail data within 8 R_M, the average of I_{M2}/I_{M3} is 1.4 ± 1.0, 1.5 ± 1.2, and 1.4 ± 1.8 for the upper, mid, and central tail regions, respectively, with the uncertainties given by the standard error in the mean of all the binned points in that region. These ratios were computed by finding the mean and standard deviation within 0.1 R_M bins along the MSO x-axis (the solid lines in Figures 1c–1e). Binned results are needed because different points were sampled during M2 and M3, and binning provides common reference points.

[12] Fantail observations (Figure 2a) of Ca were made during all three flybys as MESSENGER crossed the planet's nightside. For these observations, the spacecraft initiated a

[1]Auxiliary materials are available in the HTML. doi:10.1029/2012JE004158.

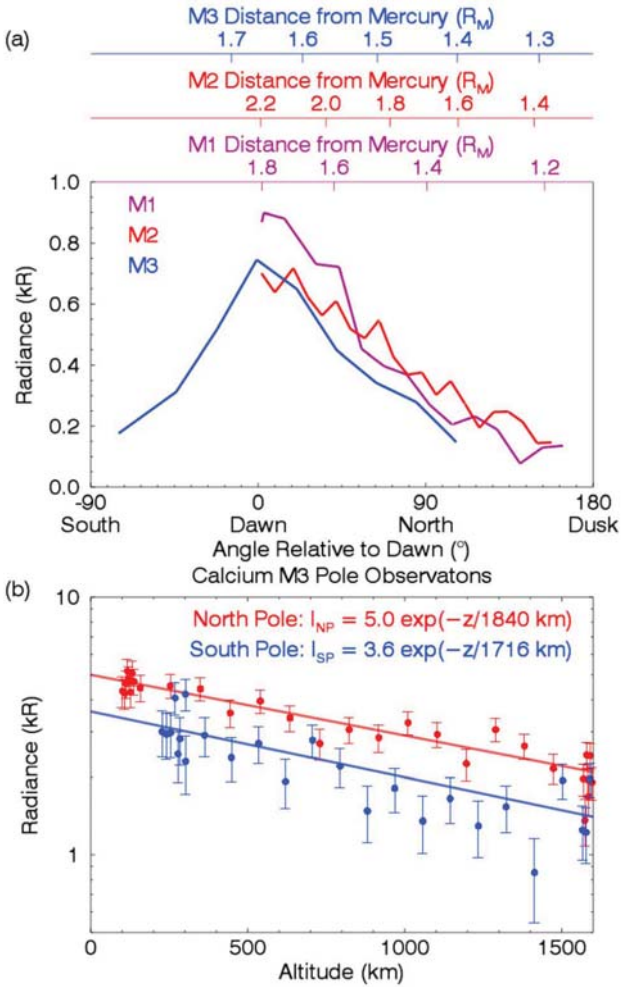

Figure 2. (a) Calcium fantail measurements from each of the MESSENGER flybys of Mercury. The bottom axes indicates the direction of the MASCS boresight relative to the equatorial dawn direction, with positive values indicating that UVVS pointed north of the equatorial plane and negative values indicating southward pointing. The top axes gives the radial distance of MESSENGER from Mercury's center. (b) Emission over Mercury's north (red) and south (blue) poles observed by UVVS during M3. Exponential fits to the data are shown by the solid lines. In the exponential fits, $z = (r - R_M)$ where r is the distance from Mercury's center and R_M is Mercury's radius.

roll maneuver that allowed the latitudinal dependence of the tail within ~2 R_M to be measured. Although the brightnesses appear to be consistent for all three flybys, a direct comparison is not possible as MESSENGER's distance from the planet (indicated by the top axes in Figure 2a) was different for each of the fantail maneuvers. A common feature of all three flybys was that the emission was brightest when pointing in the dawn (MSO $-y$) direction parallel to the equatorial plane.

[13] During M3, UVVS measured altitude profiles of Ca emission over the poles (Figure 2b) [*Vervack et al.*, 2010]. The emission within 1600 km of the surface can be approximated by the exponential $I = I_0 e^{-(r-r_0)/h}$, where r is the distance from Mercury's center; r_0 is Mercury's radius (so that $r - r_0$ is the altitude above the surface); I_0, the radiance at the surface, is 5.0 kR and 3.6 kR at the north and south poles, respectively, and h is the e-folding scale height (1840 ± 140 km and 1700 ± 200 km at the north and south poles, respectively). The exponential decrease with altitude was similar over both poles; however, $I_{0,NP}/I_{0,SP} = 1.4 \pm 0.1$, indicating a north–south asymmetry in the emission. The model simulations described below show that a small asymmetry in the source location does not affect the distribution in the fantail or tail (see Figure 10). Differences in the observing geometry over each pole cannot account for this asymmetry (demonstrated below by model simulations of the UVVS observations along the lines of sight; see auxiliary material Figure S3, which shows that an isotropic calcium exosphere does not result in a polar asymmetry). The temperature implied by these scale heights is >30,000 K or a mean energy >2.6 eV. This temperature does not take into account the fast photoionization rate for Ca (7.2×10^{-4} s^{-1}), so the actual source temperature is likely larger.

3. Exospheric Model

[14] We used a Monte Carlo model of neutral exospheres that has previously been applied to the study of the sodium distribution in Mercury's exosphere observed during the first and second MESSENGER flybys [*Burger et al.*, 2010; *Mouawad et al.*, 2011]. Packets representing collections of calcium atoms were ejected from the surface with specified spatial and velocity distributions. We assumed that all the calcium is ejected in atomic form from the surface with an initial velocity defined by a Maxwellian flux distribution, $\phi_M(v) \sim v^3 e^{-v^2/v_{th}^2}$, where v is the speed, $v_{th} = \left(\frac{2kT}{m_{Ca}}\right)^{1/2}$ is the thermal speed, k is the Boltzmann constant, and m_{Ca} is the atomic mass of a calcium atom (40.1 times the mass of hydrogen, or 6.7×10^{-23} g).

[15] *Killen et al.* [2005] suggested that calcium might be ejected in molecular form and subsequently photodissociated to produce energetic atomic Ca. CaO, one of the most likely molecular species, has a photolysis lifetime of ~200 s [*Berezhnoy and Klumov*, 2008]; therefore, the CaO scale height is <100 km, if we assume that CaO was produced by a low-energy process such as impact vaporization. Our source mechanism is consistent with this hypothesis, but because UVVS did not observe below this height we cannot distinguish between an energetic surface process launching atoms into the exosphere and an energetic atom created at low altitude in a molecular exosphere.

[16] The number of atoms represented by each packet (the "content" of the packet) is tracked during the simulation. Loss by photoionization reduces this number. The Ca photoionzation rate at 1 AU is 6.96×10^{-5} s^{-1} during normal (quiet) solar conditions (W. F. Huebner and J. Mukherjee, Photo rate coefficient database, 2011, http://phidrates.space.swri.edu). Over the course of a Mercury year, the Ca photoionization lifetime at Mercury varies between 23 and 52 min due to Mercury's changing heliocentric distance in its eccentric orbit. During the flybys, the Ca lifetimes were 29, 28, and 23 minutes for M1, M2, and M3, respectively

(Table 1). Packets that return to the surface or escape the region of interest (a sphere of radius 15 R_M centered on Mercury) are removed from the simulation.

[17] The motion of packets is governed by Mercury's gravity and radiation pressure. Because we are interested in the exosphere deep within Mercury's Hill sphere (which varies between 72 and 102 R_M over the course of a Mercury year), we ignore the effects of solar gravity. Solar photons with the energy of the resonant transitions are absorbed and almost immediately emitted, producing the isotropic, resonantly scattered emission UVVS observes. Because the photons are incident from a single direction and emitted isotropically, an atom experiences an impulse in the direction of the incident photon. The acceleration due to radiation pressure on a Ca atom is given by

$$a_r = \sum_i \frac{h g_i}{m_{Ca} \lambda_i} \quad (1)$$

where h is Planck's constant, λ_i are the resonant transitions, and g_i are the g-values of each transition. Thus, the magnitude of the radiation pressure and the resonant-scattering rate both depend on the g-values. The solar flux at the transition wavelength depends on the distance from the Sun and the radial velocity between the neutral atom and the Sun. Ca absorption in the solar atmosphere forms a deep Fraunhofer absorption line in the solar spectrum, such that when the radial velocity of the atom is near zero, the solar photon flux at the resonant wavelength is 19% of the flux when Mercury's radial velocity is maximized ($\pm$ 10.1 km s^{-1}) and the transition wavelength is Doppler-shifted into the wings of the Fraunhofer absorption line. The g-values for Ca as a function of radial velocity were computed by *Killen et al.* [2009] and are given in Table 1 for an atom at rest with respect to Mercury at the time of each flyby. Radiation pressure acts in the anti-sunward direction (MSO $-x$). Ca resonance lines at 272.2 nm and 456.7 nm are included in the radiation pressure calculation in addition to the 422.7 nm line, although combined they contribute only $\sim$1% of the total effect. The g-value is computed at each time step from the instantaneous radial velocity of the packet. For a Ca atom at Mercury, the magnitude of the acceleration due to radiation pressure is given by:

$$a_r = 0.28 \left(\frac{g_{0.352}(v_r)}{d^2} \right) \quad (2)$$

where a_r is the radiation acceleration in units of cm s^{-2}, d is the distance of Mercury from the Sun in astronomical units (AU), and $g_{0.352}(v_r)$ is the g-value at 0.352 AU as a function of the radial velocity relative to the Sun v_r for the Ca 422.7 nm transition as given in Figure 12 of *Killen et al.* [2009] in units of photons atom^{-1} s^{-1}. Because radiation pressure depends on the number of incident photons, $a_r = 0$ for atoms in Mercury's shadow.

[18] The first and second flybys occurred at similar true anomaly angles and were characterized by similar Ca lifetimes and g-values. Mercury was closer to perihelion during the third flyby (M3), and the lifetime was 20% shorter than during the first flyby. The solar flux increases with decreasing heliocentric distance, but the flux at the resonance wavelength decreases with decreasing magnitude in the heliocentric radial velocity ($|dr/dt|$); these combined effects caused the g-value to be 24% smaller during M3 than during the first flyby (M1). This outcome had two effects: the smaller radiation pressure decreased the escape rate down the tail, and calcium was intrinsically fainter during M3 than during the first two flybys (i.e., the same column of Ca produced less emission during the third flyby).

[19] The integration time for each packet was randomly chosen from a uniform distribution between the start and end times of the simulation, with the total integration time taken to be four times the Ca photoionization time (given in Table 1). The Ca density and radiance were determined by the state (position, velocity, and content) at the end of the simulation. Because the integration times for the packets are distributed between the start and end times of the simulation, some of the packets represent atoms that have just been launched from the surface, whereas some have persisted for several times the photoionization timescale and have had their content substantially reduced. The content of a packet relative to its initial content is $\exp(-t_{Sun}/\tau)$, where t_{Sun} is the time a packet spends in sunlight out of Mercury's shadow, and τ is the photoionization time. No photoionization occurs while the packet is in the planet's shadow.

4. Modeling MESSENGER Flyby Data

4.1. Isotropic Source

[20] We first consider the exosphere that results from an isotropic source of Ca (i.e., one that is uniform over Mercury's surface). Such a source allows us to evaluate the inhomogeneities in the actual source and estimate those regions on the surface that may have a greater source flux.

[21] The UVVS fantail data from all three flybys are compared in Figure 3 with model simulations for Maxwellian initial flux distributions and for temperatures ranging between 5000 and 50,000 K. The mean radiances in the models are scaled to the mean observed radiances in the entire data set from that flyby, giving estimates of the total Ca source rate (because, under the assumption of optically thin emission, radiance is linearly proportional to the source rate, all other parameters being equal).

[22] It is evident that an isotropic source is not consistent with the data. These models do not reproduce the fantail measurements for any of the flybys (Figures 3a–3c). Comparisons with the tail data from M2 are shown in Figure 4 and the complete M3 data set is shown in auxiliary material Figure S3. Figure 3d compares the approximate dawn–dusk ratio observed by UVVS with that predicted by the models. The dawn–dusk ratio was determined from the ratio of the UVVS measurement closest to dawn pointing to the measurement closest to dusk pointing. Because the spacecraft was moving toward Mercury during the fantail sequence, the dusk measurement sampled closer to Mercury than the dawn measurement during each of the three flybys; however, because the model simulates the emission along the actual UVVS lines of sight, no bias is introduced in the comparison of the model with data despite the fact that the dawn–dusk comparison is not made along directly opposing lines of sight. Because a spacecraft safing event occurred before the completion of the spacecraft roll during M3, the dawn–dusk ratios are shown only for M1 and M2. The isotropic models are poor fits to the data, as the observed

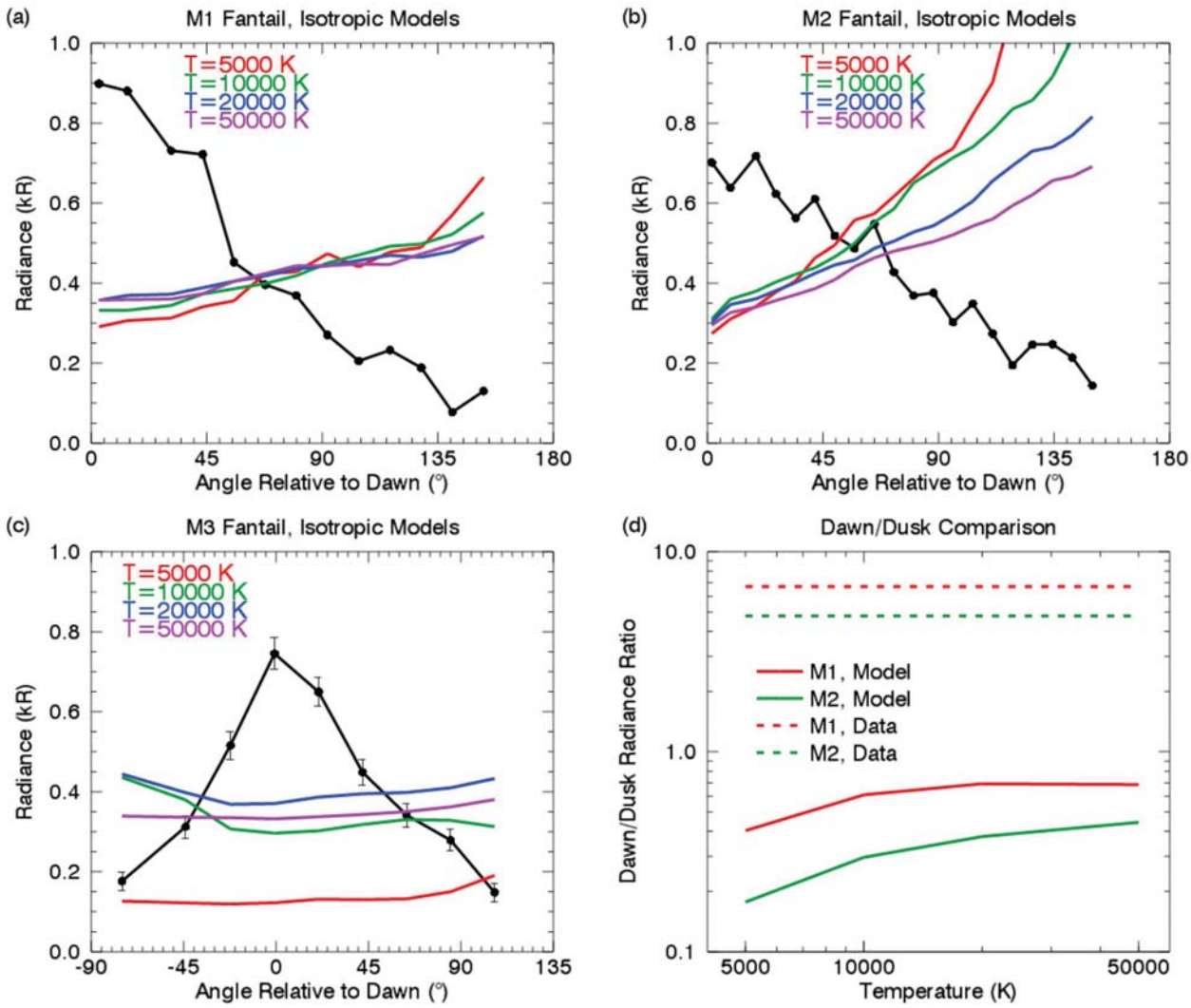

Figure 3. Comparison of fantail data from the three flybys with models having sources isotropically distributed over Mercury's surface and Maxwellian flux distributions with T = 5000 K, 10,000 K, 20,000 K, and 50,000 K. (a) Comparison of M1 data with models. (b) Comparison of M2 fantail data with models. (c) Comparison of M3 fantail data with models. (d) The observed (broken lines) and modeled (solid lines) dawn-to-dusk ratios. The method for computing this ratio is described in the text. The modeled ratios are shown as a function of source temperature. No ratio for M3 is shown because a spacecraft safing event prevented UVVS from observing in the dusk direction during that flyby.

dawn–dusk ratio is greater than 1 for both flybys (I_{dawn}/I_{dusk} = 6.7 and 4.8 for M1 and M2, respectively) and the model predicts dawn–dusk ratios <1 for source temperatures <50,000 K. The dawn–dusk ratio is <1 for these isotropic simulations because the dusk lines of sight probed deeper regions of the exosphere. The decrease in I_{dawn}/I_{dusk} at low temperatures is indicative of the smaller scale heights at these temperatures.

[23] The M2 tail measurements show another possible asymmetry in the Ca source (Figure 4). Within ~4 R_M of the planet, the model over-predicts the emission in the tail for points far from the equatorial plane (Figure 4a) relative to the emission close to the equatorial plane (Figure 4c). In other words, an isotropic model that accurately reproduces the data in the upper region does not produce enough emission in the central tail region. This mismatch suggests a source concentrated near the equator, i.e., one with a higher source flux (number of Ca atoms ejected per square centimeter) in the equatorial regions than in the polar regions. This spatial variation differs from that indicated by the simultaneous observations of Na made by UVVS, which imply increased flux of Na in the polar regions [*Burger et al.*, 2010]. This effect is not apparent in the M3 tail observations (auxiliary material Figure S3). Auxiliary material Figures S3b and S3c also indicate that the north–south asymmetry in the M3 pole data is not simply an effect of the observing geometry; if it were, the isotropic model would display a similar asymmetry over the poles. Instead, the calcium distribution itself must be asymmetric.

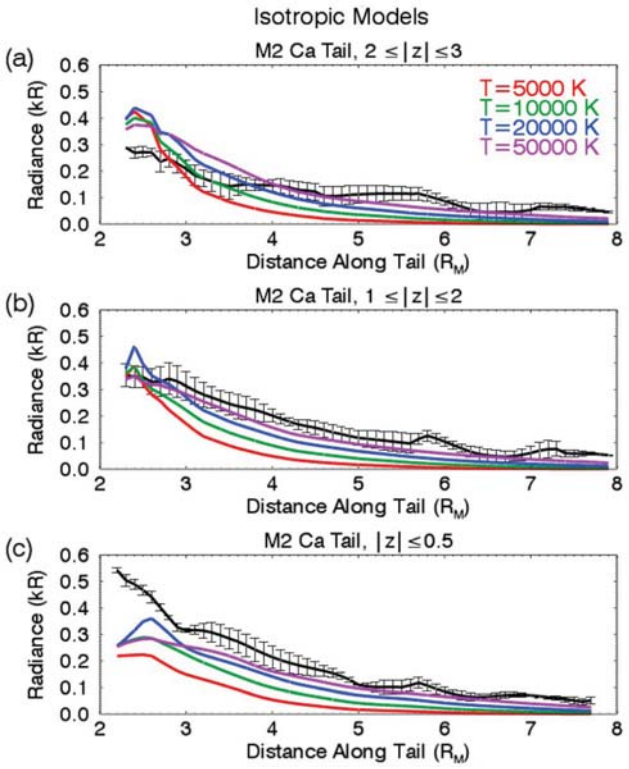

Figure 4. Comparison of M2 tail data with models featuring a source isotropically distributed over the surface and Maxwellian flux distributions with T = 5000 K, 10,000 K, 20,000 K, and 50,000 K. (a) The upper tail region. (b) The mid-tail region. (c) The central tail region.

4.2. Dawn Calcium Source

[24] The results from the isotropic models suggest a substantial dawn enhancement in the Ca source. To simulate this enhancement, we have parameterized the Ca flux from the surface as having an exponential decline with increasing angular distance from the center of the source. We define each point on the surface by its longitude λ and latitude μ relative to the subsolar point, where $\lambda = 0°$ is the subsolar meridian, $\lambda = 90°$ is the dusk meridian, and μ varies from $-90°$ at the south pole to 90° at the north pole. In MSO coordinates, a unit sphere is defined by the radius vector

$$\mathbf{r} = (x, y, z) = (\cos\lambda\cos\mu, \sin\lambda\cos\mu, \sin\mu) \quad (3)$$

The flux at each point on the surface is given by:

$$f(\lambda, \mu) = f_0 e^{(-\phi(\lambda,\mu)/\sigma)} \quad (4)$$

$$\cos\phi = \mathbf{r} \cdot \mathbf{r}_0 \quad (5)$$

where f_0 is the maximum flux from the surface, σ is the angular width of the source, and $\mathbf{r}_0$ is a vector from Mercury's center to source center. Comparisons between the models with the source centered at the dawn, equatorial point [(λ, μ) = ($-$ 90°, 0°)] and the fantail data from the three flybys are shown in Figures 5–7. The model fits to the M2 and M3 data from the mid-tail region are presented in Figure 8, and fits to the M3 polar data are in Figure 9.

[25] We can draw several conclusions regarding the nature of the Ca source from these model simulations. From the M1 comparison (Figure 5), although the data were obtained over a limited region of the exosphere, we conclude (a) the temperature of the source was ≥20,000 K, and (b) the width of the source region is ∼20°. For the low-temperature sources (5000 K and 10,000 K, Figures 5a and 5b), there is too little escaping material as evidenced by the "turn-up" when pointed at dusk (line-of-sight angles approaching 180° relative to dawn). Even though all the Ca is released from the dawn region in this model, Ca atoms with an initial speed $\lesssim$4.3 km s^{-1}, the escape speed from Mercury, are pulled back toward the planet and seen over the dusk hemisphere. Some Ca escapes, pushed into the tail by radiation pressure, but the combined forces of solar radiation and gravity globally redistribute most of the material. The best fits to the M1 data are with (T, σ) = (20,000 K, 20°) and (T, σ) = (50,000 K, 25°).

[26] Models of the M2 fantail region (Figure 6) give results similar to those for M1, although the tail measurements (Figure 8a) give additional constraints. The lower-temperature models (T = 5000 K and T = 10,000 K) fail to send enough Ca into the tail past ∼3 R_M and do not reproduce the observed dawn–dusk asymmetry except for the smallest (σ = 10°) source region. The tail data are sensitive to the source temperature, but not to the size. The fantail data, however, are sensitive to both parameters. A source with T = 20,000 K and σ = 20° is a good fit to the fantail observations, as it is for the M1 fantail data, but the tail data require a more energetic source. The best fit to the entire M2 data set is a source with T = 50,000 K and σ = 25°–30°. Such a source produces the appropriate dawn–dusk ratio in the fantail (Figure 6) and enough Ca in the tail at distances <8 R_M (Figure 8a). This source is also a good fit to the M1 data.

[27] The M3 coverage was improved over the M2 observations owing to the addition of the polar scans and the longer spacecraft roll during the fantail sweep. For M3, the 5000 K and 10,000 K models fail for two reasons. First, they do not send enough material into the tail (Figures 7a and 7b); and second, the scale heights above the poles are too small (Figure 9). However, in contrast to the situation for M1 and M2, it is possible to fit the fantail data with the colder (i.e., less energetic) sources – still narrowly confined to the equator – because the dawn–dusk asymmetry was not measured during this flyby as a result of the spacecraft safing event.

[28] All three phases of the M3 data set (tail, fantail, and polar scans) are well fit by a 50,000 K source with σ = 20°–25° (Figure 7 and auxiliary material Figure S4). This source reproduces the dawn enhancement seen in the fantail, the tail data within 8 R_M of Mercury, and the Ca scale height observed over both poles. The one feature that is not captured with this model is the north–south asymmetry in brightness observed over the poles and, to a lesser extent, in the fantail data. This asymmetry suggests a northward offset in the source of ∼5–10° in latitude (Figure 10). The distributions in the tail during M2 and M3 were not sensitive to small latitudinal changes in the source (e.g., Figures 10d–10f).

[29] The data from all three flybys are consistent with a source having (T, σ) = (50,000 K, 25°). The Ca source rate, S, is computed by integrating equation (4) over Mercury's surface: $S = \int f(\lambda,\mu) d\Omega$, where S is measured in Ca atoms ejected over the surface per second and f_0 in equation (4) is

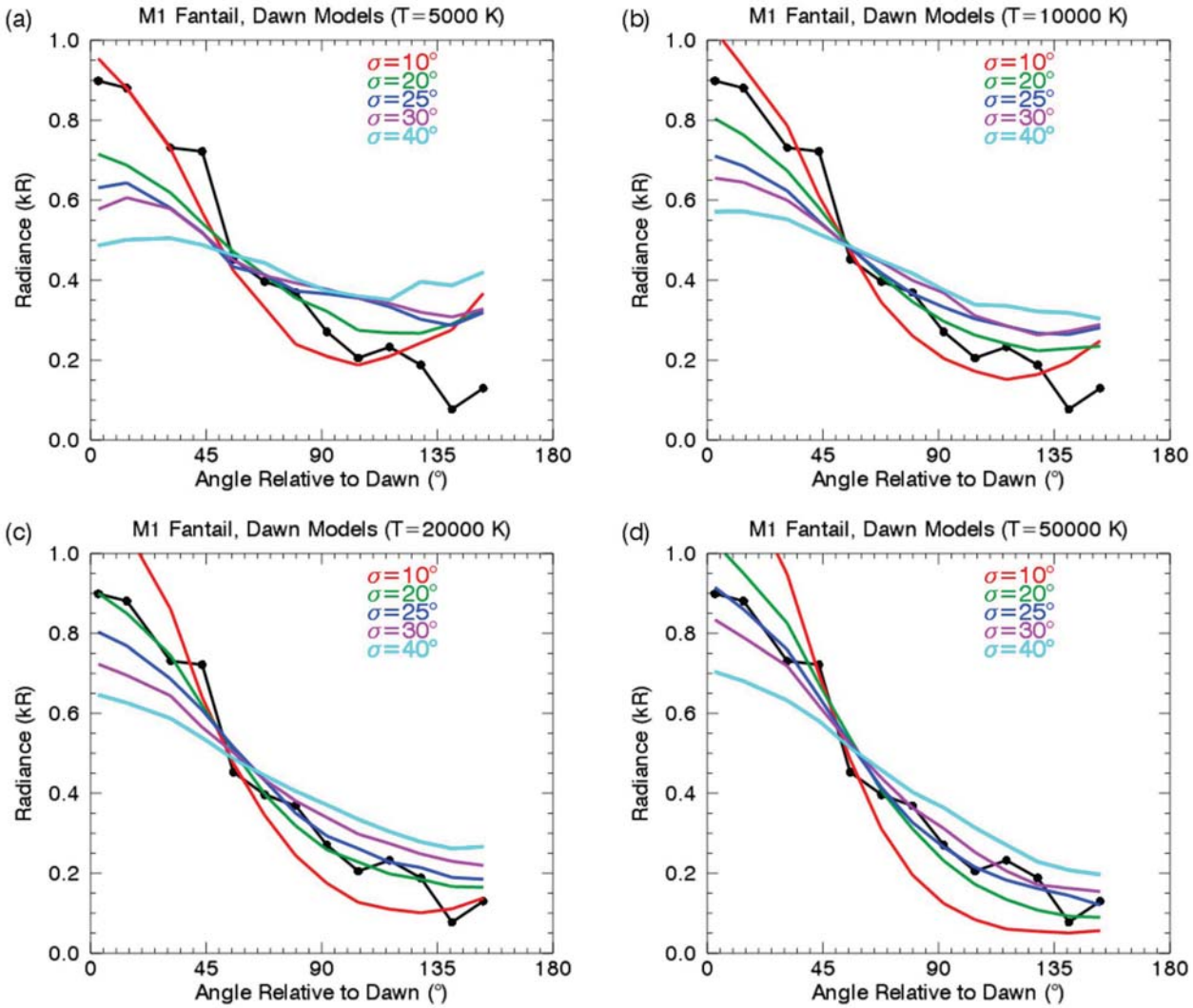

Figure 5. Fits to the M1 Ca observations with a source centered at the dawn equatorial point. Fits are shown for the source width varying between 10° and 40° and source temperatures of (a) 5000 K, (b) 10,000 K, (c) 20,000 K, and (d) 50,000 K.

measured in $cm^{-2}\ s^{-1}$. Table 2 lists the source rates derived from selected model parameters that best fit the data. The mean estimated source rate during all three flybys is $1.5 \pm 0.3 \times 10^{23}$ Ca s^{-1}, corresponding to a maximum surface flux of $2.5 \pm 0.5 \times 10^{6}$ Ca $cm^{-2}\ s^{-1}$. The source rates during M2 and M3 were approximately equal, whereas the M1 source rate was ~70% that of M2 and M3. The source may be offset ~ 5–10° north of the equator, although the UVVS observations were sensitive to a possible offset only during M3.

4.3. Constraints on a Cold Ca Source

[30] In the preceding analysis, we assumed that the data can be fit by a single-temperature model. In this section we evaluate the limits on a possible cold Ca source.

[31] During the first two flybys, UVVS was not sensitive to a low-energy, non-escaping component of the Ca exosphere because the UVVS lines of sight did not probe sufficiently close to the planet. Simulations of both a global, isotropic Ca source and a source concentrated at dawn with a temperature < 2000 K produce no emission along the M1 and M2 lines of sight. From these data, therefore, it is not possible to place constraints on a possible low-temperature source.

[32] The observations over the poles during M3 were those best suited for determining the contribution of a possible low-energy component to the exosphere. Because a low-temperature ($T \lesssim 2000$ K) source would provide no Ca to the regions viewed by the tail and fantail lines of sight, we assume that the best-fit dawn source [(T, σ) = (50,000 K, 20°), and displaced northward 5° from the equator] supplied the Ca to these regions. This same model is also a good fit to the pole data; therefore a cold source must have a flux sufficiently small that its contribution would not adversely affect the fits of the combined hot and cold sources. We find that a globally isotropic cold component of 1000 K, 2000 K, or 5000 K could have a maximum source rate of 7×10^{22} s^{-1}, 5×10^{22} s^{-1}, or 3×10^{22} s^{-1}, respectively, without significantly affecting the fit to the data

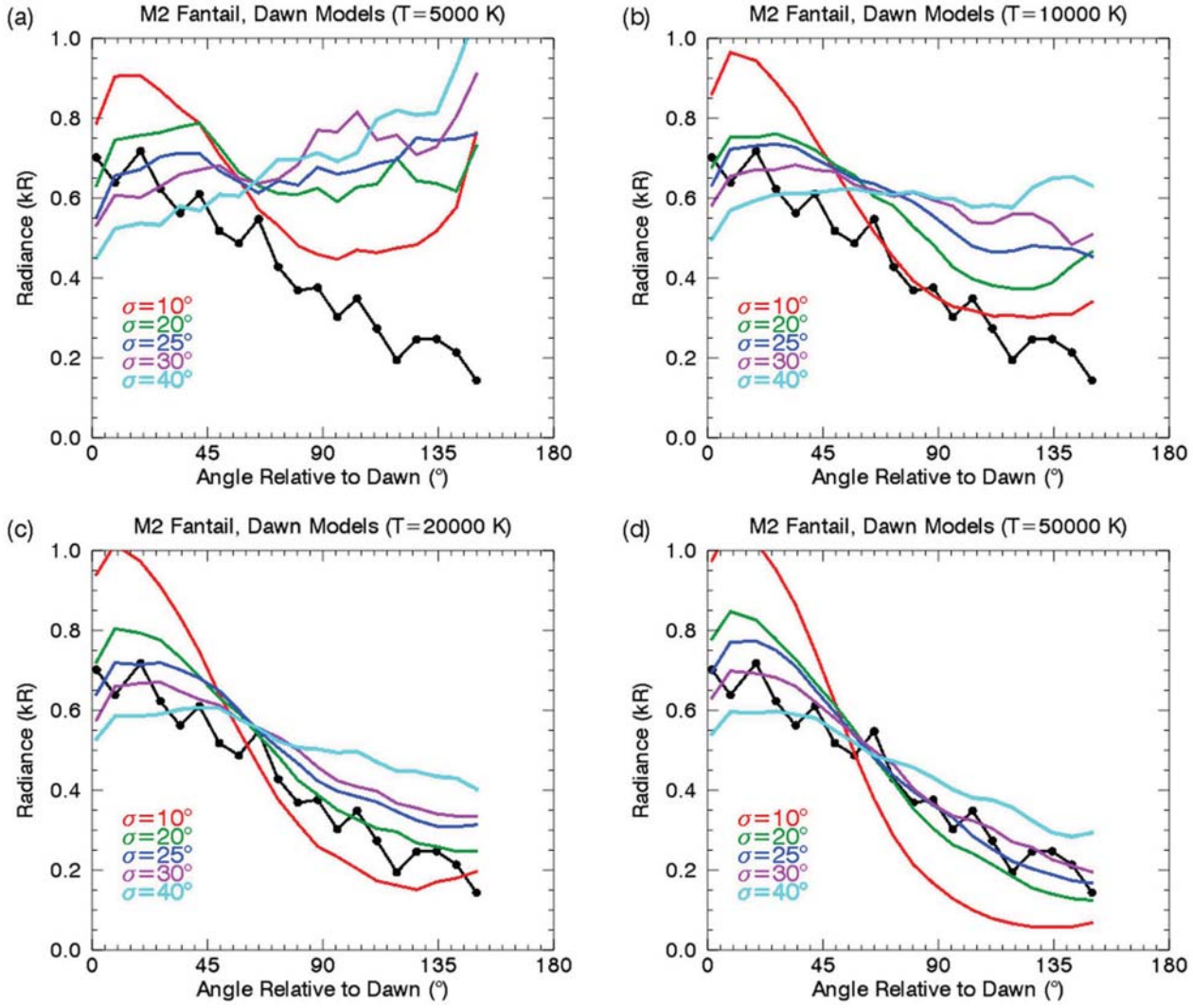

Figure 6. Fits to the M2 Ca fantail observations with a source centered at the dawn equatorial point. Fits are shown for the source width varying between 10° and 40° and source temperatures of (a) 5000 K, (b) 10,000 K, (c) 20,000 K, and (d) 50,000 K.

provided by the hot source alone. Similarly, if the cold component has the same spatial distribution as the hot component, the maximum source rate could be 1×10^{23} s^{-1}, 6×10^{22} s^{-1}, or 4×10^{22} s^{-1} for 1000 K, 2000 K, or 5000 K sources.

[33] The Ca production rate from micrometeoroid impact vaporization has been estimated from the results of several workers [e.g., *Cintala*, 1992; *Borin et al.*, 2010]. The Ca source rates calculated in these studies vary from 3.9×10^{23} s^{-1} to 3.5×10^{26} s^{-1} (summarized by *Borin et al.* [2010]) and depend on the micrometeoroid flux to the surface, the relative fractions of the impactor flux supplied from the asteroid belt versus cometary dust, the assumed surface composition, and the microphysics of impact plume production. Our upper limits on the exospheric source due to impact vaporization (if the isotropic source is produced entirely by impacts) is < 0.2 times the smallest of these estimates if the vapor is produced at 1000 K and < 0.1 times the smallest estimate if the vapor is 5000 K. These results suggest that further study of the impact vapor production rate at Mercury and a better understanding of the cold, near-surface component of the exosphere are needed to understand this exospheric source.

5. Results From the MESSENGER Orbital Phase

[34] UVVS began regular observations of Ca in Mercury's exosphere on 29 March 2011. We have applied the results from the flybys to the first seven MESSENGER orbits during which UVVS obtained observations, covering the first four days of orbital science observations, to determine whether the Ca source remained in the dawn equatorial region. Table 1 lists the start time for each orbit considered (measured from MESSENGER apoapsis) along with Mercury's heliocentric distance and radial velocity.

[35] A comparison of the UVVS data from the first science orbit (orbit 22) with isotropic models and models having a dawn source with $\sigma = 25°$ is shown in Figure 11. The local

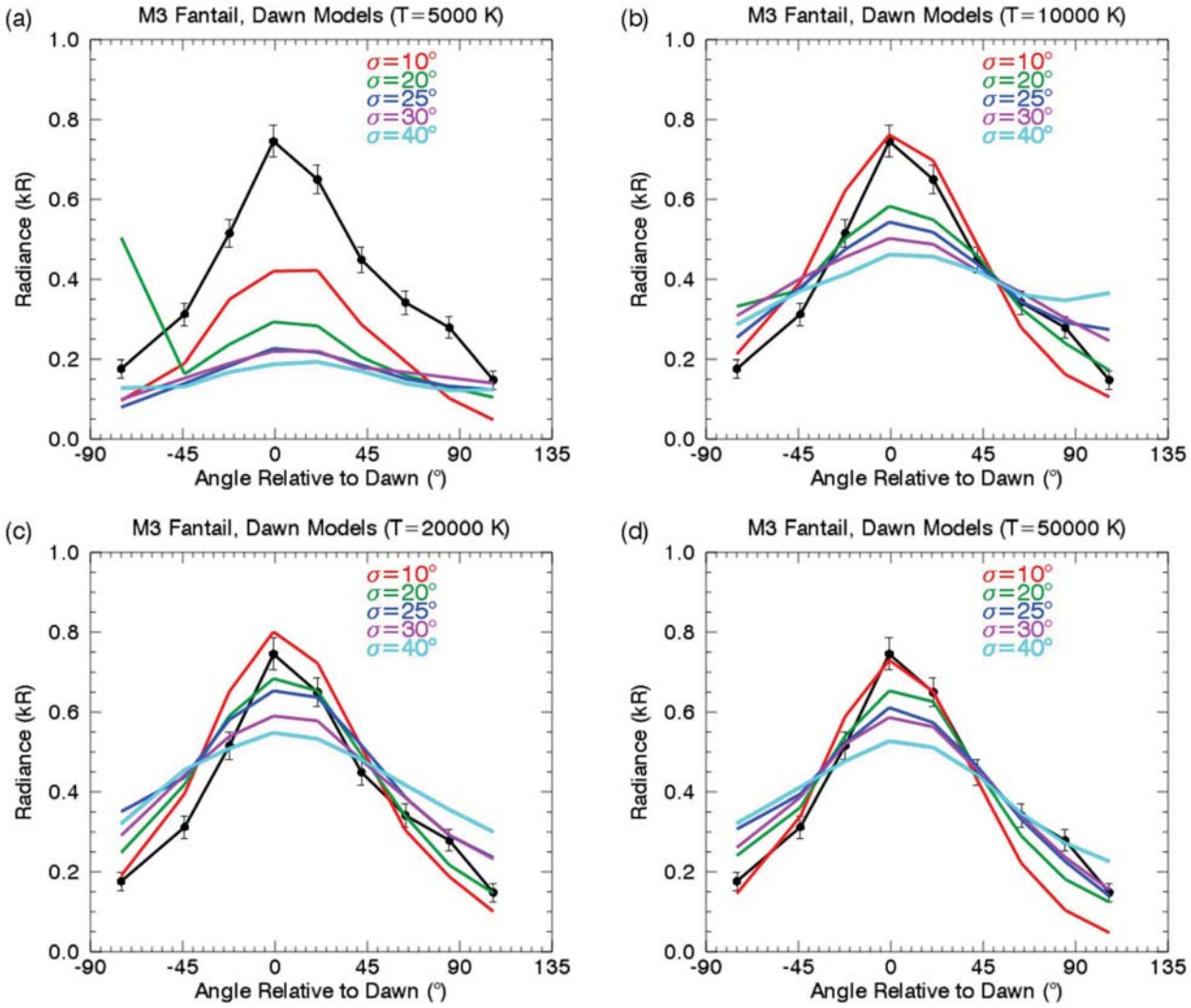

Figure 7. Fits to the M3 Ca fantail observations with a source centered at the dawn equatorial point. Fits are shown for the source width varying between 10° and 40° and source temperatures of (a) 5000 K, (b) 10,000 K, (c) 20,000 K, and (d) 50,000 K.

time and distance from Mercury's center of the point closest to Mercury's surface observed in each UVVS spectrum (the tangent point) is indicated in Figure 11a. Local times between 6 hours and 18 hours are over Mercury's dayside. Tangent distances <1 indicate that the line of sight intersected Mercury's surface. Only spectra with a signal-to-noise ratio (SNR) >2 and for which the lines of sight do not intersect the surface are included in the model fits to the data. Auxiliary material Figures S5–S10 compare the data and models for orbits 23–28 in the same format.

[36] By inspection, it can be seen that the isotropic models at the three temperatures presented (5000 K, 20,000 K, and 50,000 K) fail to fit the data from the first seven orbits. The orbital data are most consistently fit with a dawn source having $\sigma = 25°$ and a temperature ≥20,000 K. This outcome is shown quantitatively in Figure 12a, which gives the minimum χ^2-statistic for the three dawn-source models considered here, computed from

$$\chi^2 = median\left[\frac{(D_i - SM_i)^2}{s_i^2}\right] \quad (6)$$

where S is the Ca source rate, and D_i, s_i, and M_i are the observed radiance, uncertainty in the radiance, and modeled radiance per unit source rate for UVVS line of sight i, respectively. We have used this modified χ^2 rather than the usual χ^2-statistic because (a) outlying data points can skew the fit to the data, and (b) the model employed here is fairly simple. For these fits, we have found the minimum χ^2 by varying only a single free parameter – the total source strength, S. A more sophisticated model should include additional free parameters such as source temperature (T), source width (σ),

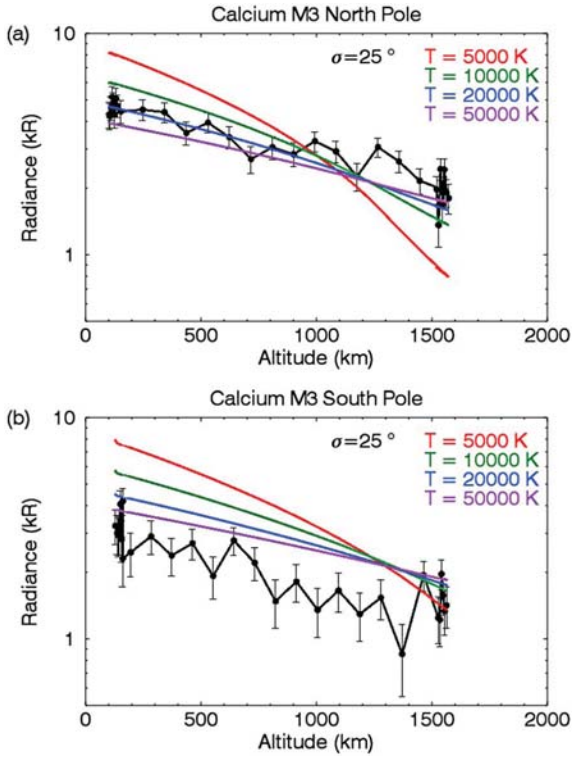

Figure 8. Fits to the (a) M2 and (b) M3 tail data using a dawn equatorial source with $\sigma = 25°$ and source temperature varying from 5000 K to 50,000 K.

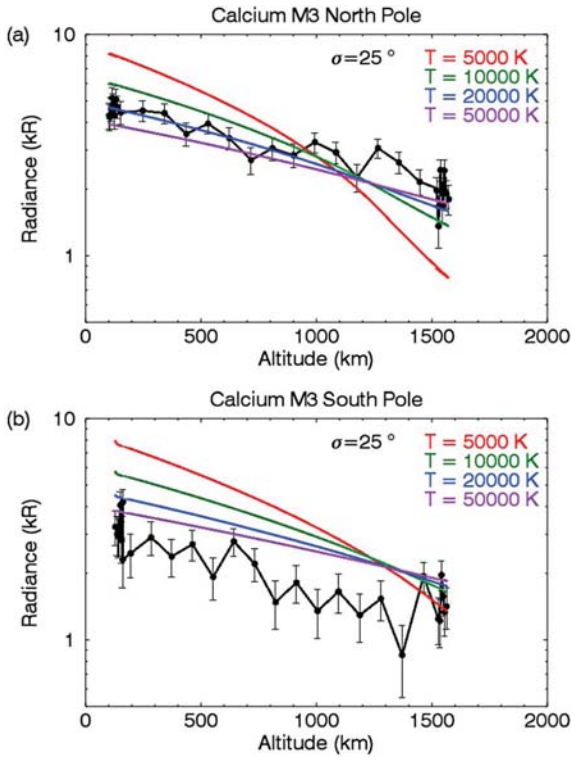

Figure 9. Fits to the M3 (a) north pole and (b) south pole data for a dawn equatorial source with $\sigma = 25°$ and source temperature varying from 5000 K to 50,000 K.

Table 2. Summary of Best-Fit Models for a Dawn Source of Ca in Mercury's Exosphere

Orbit	(λ_0,μ_0)	σ (deg)	S (s^{-1}) (T = 20,000 K)	S (s^{-1}) (T = 50,000 K)
M1	(−90,0)	20	1.1×10^{23}	poor fit
M1	(−90,0)	25	poor fit	1.2×10^{23}
M2	(−90,0)	25	poor fit	1.6×10^{23}
M2	(−90,0)	30	poor fit	1.5×10^{23}
M3	(−90,5)	20	poor fit	1.8×10^{23}
M3	(−90,5)	25	poor fit	1.7×10^{23}
22	(−90,0)	25	1.7×10^{23}	2.4×10^{23}
23	(−90,0)	25	1.8×10^{23}	2.6×10^{23}
24	(−90,0)	25	1.5×10^{23}	2.3×10^{23}
25	(−90,0)	25	2.0×10^{23}	2.6×10^{23}
26	(−90,0)	25	1.6×10^{23}	2.0×10^{23}
27	(−90,0)	25	1.9×10^{23}	2.5×10^{23}
28	(−90,0)	25	1.7×10^{23}	2.2×10^{23}

and the location of the source center on the surface (λ_0, μ_0). For the purposes of this paper, we wish only to show that the dawn Ca source used to explain the UVVS flyby data is also more consistent with the data obtained during the early MESSENGER orbits than an isotropic Ca source.

[37] The source rate (Figure 12b and Table 2) during this period was approximately constant, with $S = 1.7 \pm 0.2 \times 10^{23}$ s^{-1} if $T = 20{,}000$ K and $S = 2.3 \pm 0.2 \times 10^{23}$ s^{-1} if $T = 50{,}000$ K. This behavior suggests the morphology of the source on the surface was similar to that seen during the flybys with an ~30% increase in the source strength compared with M2 and M3. We have not evaluated the extent to which the fits could

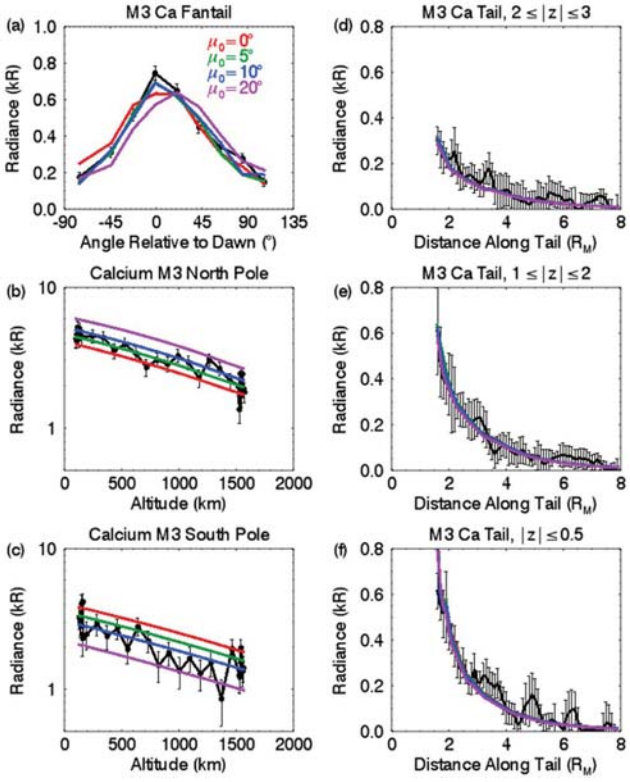

Figure 10. Effect on M3 models of shifting the Ca source northward between 0 and 20° latitude. The Ca source for all models has (T, σ) = (50,000 K, 25°).

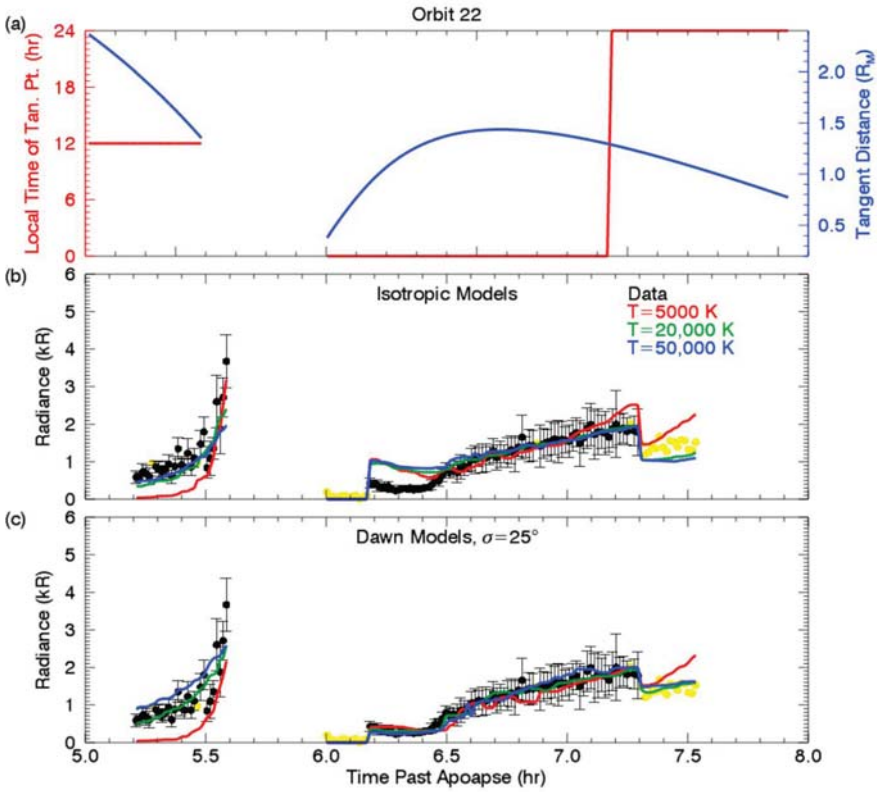

Figure 11. Comparison of UVVS data and model simulations from MESSENGER orbit 22. (a) UVVS observing geometry showing the local time (red) and distance from Mercury's center (blue) to the point closest to Mercury's surface along the UVVS line of sight (the tangent point). (b) Comparison between data and isotropic models with temperatures of 5000 K (red), 20,000 K (green), and 50,000 K (blue). Data points in black, shown with one-standard-deviation errors, are included in the χ^2-fitting. Yellow data points have either a signal-to-noise ratio <1 or a line of sight intersecting Mercury's surface and are not included in the fits. (c) Comparison between data and dawn-source models centered on the dawn equatorial point with $\sigma = 25°$.

be improved by variations in the size, temperature, and location on the surface of the dawn source region. To first order, however, the location and extent of the source were the same during the flybys and first seven orbits and were fixed in Mercury local time rather than associated with a particular geologic feature or the surface composition.

6. Discussion

[38] We have presented models of UVVS observations of Ca in Mercury's exosphere. The data from the three MESSENGER flybys of Mercury and the first four days of the MESSENGER orbital observations point to a persistent, high-energy source of Ca located in Mercury's dawn, equatorial region. We modeled the data under the assumption that all the Ca is emitted from a region on the surface centered at the dawn, equatorial point (displaced northward by ~5–10° latitude during M3). The source flux in the model decreases exponentially with distance from the source center with an *e*-folding width of ~25°, corresponding to a circle on the surface of radius ~1100 km. If the size, mean energy, and location of the source remained constant, then the source strength increased from 1.2×10^{23} Ca s^{-1} during the first MESSENGER flyby in January 2008 to 2.3×10^{23} Ca s^{-1} at the beginning of the primary MESSENGER orbital mission phase in March 2011. During the period 29 March – 1 April 2011, variations about the mean source rate showed no resolvable temporal trends; i.e., the orbit-to-orbit variations about the mean source rate of $\sim 2 \times 10^{23}$ Ca s^{-1} were smaller than the mean uncertainties in our the uncertainty in our one-parameter fits. The standard deviations about the mean source rates were 0.19×10^{23} s^{-1} and 0.25×10^{23} s^{-1} for the 20,000 K and 50,000 K sources, respectively, compared with mean uncertainties of 0.48×10^{23} s^{-1} and 0.41×10^{23} s^{-1}.

[39] Previous workers have concluded that Ca is emitted from the surface at a high temperature [*Bida et al.*, 2000; *Killen et al.*, 2005, 2009]. Our results are consistent with this conclusion: we have constrained the temperature to be ≳20,000 K and likely ~50,000 K. Observations close to the planet are equally well fit by sources with temperatures of 20,000 K and 50,000 K, but not 10,000 K; however, observations of the Ca tail far from the planet (≳3 R_M from Mercury's center) over the nightside made during M2 and M3 require the higher source temperature. UVVS cannot observe this far from Mercury during the orbital phase;

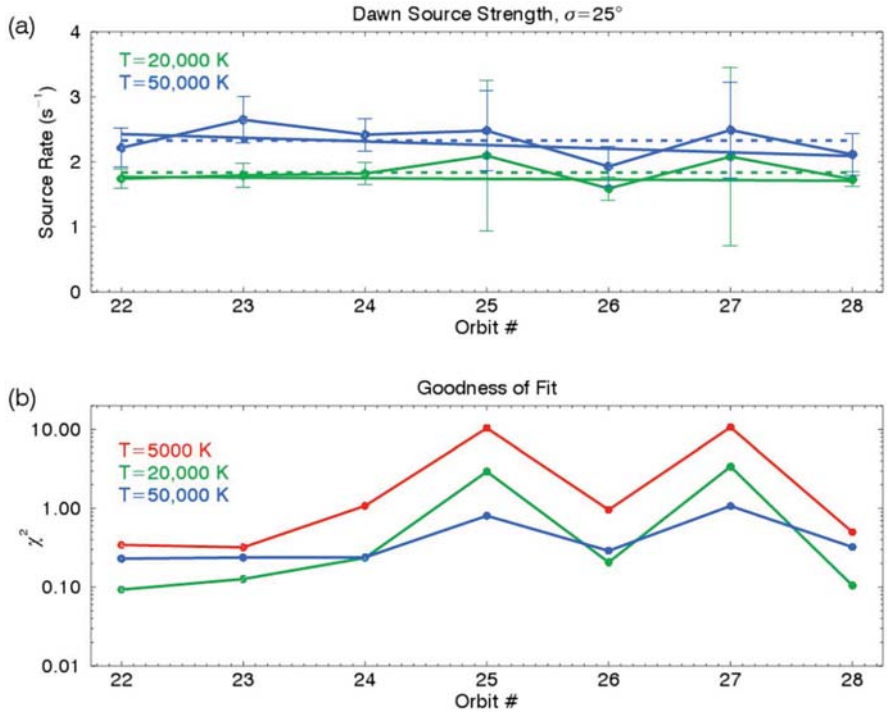

Figure 12. (a) Best-fit source strength for MESSENGER orbits 22–28 for a dawn model with $\sigma = 25°$ and $T = 20{,}000$ K (green), and $T = 50{,}000$ K (blue). The solid lines show linear fits to the results; the broken lines indicate the mean source rate at each temperature. (b) Modified χ^2-statistic described in the text for orbits 22–28 for 5000 K (red), 20,000 K (green), and 50,000 K (blue) sources.

consequently, we cannot constrain the source temperature as precisely with data obtained in orbit as we did during the flybys. We have assumed in this work that Ca was ejected with a Maxwellian flux distribution. Although this assumption may not be valid, the temperatures we derived are indicative of the mean energy of the actual flux distribution.

[40] We have also placed limits on a possible cold source of Ca due either to impact vaporization by micrometeoroids or the process acting in the dawn region that produces the energetic Ca, regardless of what that process may be. A cold ($\lesssim$5000 K) source would have contributed only to the emission over the poles that was observed during M3; a higher-energy source is required to reach the distances measured during the fantail and tail observations. The pole data are well fit by the energetic source, so we have determined the upper limit on cooler sources by estimating the source rate of a cold component that would perturb the fit of the combined cold and hot sources. Our estimates of the isotropic cold source rate are below published estimates of the Ca production rate from impact vaporization [*Borin et al.*, 2010], implying that either (a) atomic Ca is produced at a lower rate than predicted by the models, or (b) Ca is produced in impact vapor plumes at a temperature $\lesssim$1000 K. The colder the vapor, the more Ca could have been produced without contributing to the observed emission. We do not believe that substantial molecular Ca production in impact plumes is consistent with our data. Ca-bearing molecules would either condense or dissociate to produce hot Ca, a scenario we ruled out with isotropic models in Section 4.1.

[41] Energetic Ca can be produced by several mechanisms. Ion sputtering and electron-stimulated desorption (ESD) are capable of ejecting both atomic and molecular Ca from the surface at high speeds [*Johnson*, 1990; *Madey et al.*, 1998]. *Killen et al.* [2005] proposed that high-temperature atomic Ca can be produced from the dissociation of molecular Ca (CaX, possibly in the form CaO or CaS). Data from the MESSENGER X-Ray Spectrometer (XRS) show a correlation between S and Ca on the surface suggesting the presence of Ca-bearing sulfides and a possible source of exospheric CaS [*Weider et al.*, 2012]. However, the Ca abundance is 2–3 times the S abundance [*Nittler et al.*, 2011], and other molecular species are possible. Because these molecules photodissociate close to the surface and the observations utilized here do not probe these lowest altitudes, our model cannot currently determine whether the Ca is ejected from the surface in atomic or molecular form.

[42] A dawn–dusk asymmetry in the exospheric density is not unique to Ca. Although the MESSENGER flybys did not show evidence of a dawn enhancement in Na, a diurnal asymmetry has previously been seen by ground-based observers [e.g., *Sprague et al.*, 1997; *Schleicher et al.*, 2004; *Potter et al.*, 2006]. *Potter et al.* [2006] found that the dawn–dusk Na emission asymmetry varies over the course of a Mercury year. Moreover, observations of the 2006 Mercury solar transit found no evidence of a dawn enhancement, in contrast to the finding of *Schleicher et al.* [2004] from similar observations made during the 2003 transit.

[43] *Sprague* [1997] proposed a mechanism for an enhanced exospheric source of Na at the dawn terminator: magnetospheric Na^+ ions are implanted and neutralized on the nightside surface and then desorbed when they rotate into sunlight. This model is consistent with Na observations by *Schleicher*

et al. [2004] showing a small scale-height enhancement (~150 km, equivalent to a 1500 K source) over the dawn hemisphere. Similarly, Ca^+ photoions precipitating onto the surface could supply Ca to the nightside. Some observations suggest that Ca^+ ions precipitate onto the nightside. UVVS documented Ca^+ over Mercury's nightside in a small region located ~ 2–3 R_M from the planet's center and centered in the equatorial plane [*Vervack et al.*, 2010]. MESSENGER has also observed examples of extreme loading and unloading events in Mercury's magnetotail indicative of intense magnetospheric substorms [*Slavin et al.*, 2010]. During substorms, plasmoids can be ejected both down the tail and toward the nightside surface. The UVVS measurements suggest that if plasmoids impact the surface, they might contain Ca^+. These ions may sputter material directly, although we see no evidence that a detectable amount of Ca is sputtered from the nightside. However, the Ca^+ implanted on the surface provides a Ca source to be liberated as it rotates into sunlight. The mechanism by which it is ejected is uncertain, as it depends on how the Ca is bound to the surface. Ca or CaX might desorb, but their production mechanism from precipitating Ca^+ ions and binding state to the surface are not known.

[44] An alternate proposal, suggested by *Mura et al.* [2009] and *Leblanc and Johnson* [2010], explained this asymmetry by thermally driven migration of Na from the dayside to the nightside, where it becomes cold-trapped until the surface rotates into sunlight. This mechanism is not as efficient at redistributing the refractory species Ca as it is for the volatile Na. Ca sticks to the surface everywhere and is less likely to be photo- or thermally desorbed on the dayside, limiting its mobility. Essentially, the entire surface acts as a cold-trap such that Ca atoms are no more likely to become trapped on the nightside than on the dayside. In addition, the short photoionization time implies that Ca ejected on the dayside would not travel far before being ionized and picked up by the solar wind. Similarly, CaX produced on the dayside would photolyze before it could travel far from its production site.

[45] An additional weakness of both these hypotheses is that they require a persistent Ca source either from recycled photoions or dayside desorption. Approximately 50% of the photoions are picked up by the solar wind and lost down the tail, so the surface reservoir would be quickly depleted. Another source of Ca is thus needed to replenish the supply. Meteoroid impact vaporization may supply the required Ca, although we have shown that the production rate of Ca at temperatures >1000 K is too low to supply the observed Ca. If a large amount of Ca were produced in colder vaporization plumes, it would not have been detected by UVVS. It also could not be transported to the nightside in the manner described by *Mura et al.* [2009] and *Leblanc and Johnson* [2010] for the reasons given above. On the nightside, however, CaX produced in impact plumes would not photodissociate or escape, but instead would build up on the surface. In this scenario, CaX is produced everywhere and photodissociated Ca is produced everywhere on the dayside, but observable amounts of Ca are produced only over the dawn hemisphere. The CaX concentration on the surface would be greatest just before dawn, having built up slowly over the long Mercury night. Neither the CaX desorption mechanism nor the manner by which the CaX is bound to the surface is clear.

[46] If the dawn source of Ca is Ca or Ca-bearing molecules desorbing as they rotate into sunlight, one would expect there to be a seasonal variation in the Ca source rate, because the terminator does not move across Mercury's surface at a constant rate and even reverses for a short period when Mercury is near perihelion. When this fact is taken into account, the Ca data presented here do not appear to be consistent with material vaporizing at dawn. Table 1 gives the rate of change of the subsolar longitude at the time of the flybys and the orbits studied here. If the primary source of dawn Ca was material on the surface desorbing in sunlight, then M1 and M2 would have comparable source rates and the source would have been greatly reduced during M3 when the Sun appeared to stand still in the sky. The fact that the M3 source was at least as strong as the M2 source suggests that UVVS did not see material from the nightside desorbing when emerging into sunlight. However, analysis of data over multiple Mercury years is needed to better constrain the seasonal variability in the source rate.

[47] Models of the interaction of the solar wind with Mercury's magnetic field predict proton and heavy solar wind ion precipitation onto the surface [e.g., *Benna et al.*, 2010]. These precipitating ions have been proposed as a source for exospheric Na by direct sputtering [*McGrath et al.*, 1986], chemical sputtering followed by PSD [*Potter*, 1995; *Mura et al.*, 2009], or ion-enhanced diffusion followed by PSD [*Sarantos et al.*, 2010; *Burger et al.*, 2010]. Na often shows polar enhancements in its emission [*Potter and Morgan*, 1990; *Schleicher et al.*, 2004; *Killen et al.*, 2007; *McClintock et al.*, 2008], which are likely caused by one or more of these ion precipitation effects; however, high-latitude emission is noticeably absent in the Ca observations compared with equatorial regions. Na observations made during M1 and M2 exhibited high-latitude emission associated with ion precipitation [*Burger et al.*, 2010], although the observations were made in a region populated by atoms that had been pushed into the tail by solar radiation pressure. Ca produced by solar wind precipitation would not be pushed as far back into the tail due to the short photoionization lifetime and weaker radiation pressure. During the orbital phase, UVVS may have observed regions on the dayside open to precipitating ions, although we cannot be certain without magnetospheric models using the appropriate IMF conditions. However, while we cannot rule it out, our models of the dawn source do not appear to indicate an additional component from sputtering on the dayside.

[48] *McLain et al.* [2011] proposed that ESD is a possible source of exospheric neutrals and ions. Hybrid simulations of electron transport and precipitation in Mercury's magnetosphere suggest that electrons do precipitate at the dawn equatorial point [*Schriver et al.*, 2011]. Although electron precipitation might eject Ca and CaX from the surface, we identify two problems with this hypothesis as an explanation for the observed Ca emission. First, the models of *Schriver et al.* [2011] predict electron precipitation onto other regions of the surface that show no evidence of Ca emission. Second, we have shown that the Ca source size and rate are stable on timescales of days, whereas the magnetosphere varies on time scales of seconds to hours [*Slavin et al.*, 2010, 2012]. Because the Ca photoionization lifetime is ~0.5 h, we would expect orbit-to-orbit variations in the Ca exosphere unless the mean electron precipitation rate (averaged over this time) is constant. Although such constancy is possible, the ion precipitation flux fluctuates on short timescales [*Benna et al.*, 2010] and day-to-

day variability in the Na polar enhancements has been observed [*Killen et al.*, 2007], suggesting magnetospheric variability.

[49] Future work should concentrate on determining the day-to-day variability in the energetic Ca source by modeling the UVVS data from each MESSENGER orbit separately to determine the source size, location on the surface, and temperature. Modeling the source variation with time will better constrain the source mechanism. Searches for cold and isotropic components should be continued to understand all possible mechanisms that contribute to Mercury's exosphere. Moreover, improvements to models of the molecular component of the exosphere should be made to determine the limits on possible molecular sources of Ca.

[50] **Acknowledgments.** The authors thank Tim Cassidy and Sean Solomon for their many helpful discussions and comments in the preparation of this manuscript. The MESSENGER project is supported by the NASA Discovery Program under contracts NAS5-97271 to The Johns Hopkins University Applied Physics Laboratory and NASW-00002 to the Carnegie Institution of Washington. MHB is supported for this work by NASA grant NNX10AT37G.

References

Benna, M., et al. (2010), Modeling of the magnetosphere of Mercury at the time of the first MESSENGER flyby, *Icarus*, *209*, 3–10, doi:10.1016/j.icarus.2009.11.036.

Berezhnoy, A., and B. Klumov (2008), Impacts as sources of the exosphere on Mercury, *Icarus*, *12*, 70–76, doi:10.1016/j.icarus.2008.01.005.

Bida, T. A., and R. M. Killen (2011), Observations of Al, Fe and Ca^+ in Mercury's exosphere, paper presented at EPSC-DPS Joint Meeting, EPSC, Nantes, France.

Bida, T. A., R. M. Killen, and T. H. Morgan (2000), Discovery of calcium in Mercury's atmosphere, *Nature*, *404*, 159–161, doi:10.1038/35004521.

Borin, P., M. Bruno, G. Cremonese, and F. Marazri (2010), Estimate of the neutral atoms' contribution to the Mercury exosphere caused by a new flux of micrometeoroids, *Astron. Astrophys.*, *517*, A89, doi:10.1051/0004-6361/201014312.

Broadfoot, A. L., S. Kumar, M. J. S. Belton, and M. B. McElroy (1974), Mercury's atmosphere from Mariner 10: Preliminary results, *Science*, *185*, 166–169, doi:10.1126/science.185.4146.166.

Broadfoot, A. L., D. E. Shemansky, and S. Kumar (1976), Mariner 10—Mercury atmosphere, *Geophys. Res. Lett.*, *3*, 577–580, doi:10.1029/GL003i010p00577.

Burger, M. H., R. M. Killen, R. J. Vervack Jr., E. T. Bradley, W. E. Mcclintock, M. Sarantos, M. Benna, and N. Mouawad (2010), Monte Carlo modeling of sodium in Mercury's exosphere during the first two MESSENGER flybys, *Icarus*, *209*, 63–74, doi:10.1016/j.icarus.2010.05.007.

Cintala, M. J. (1992), Impact-induced thermal effects in the lunar and Mercurian regoliths, *J. Geophys. Res.*, *97*, 947–973.

Johnson, R. E. (1990), *Energetic Charged-Particle Interactions With Atmospheres and Surfaces*, 232 pp., Springer, Berlin.

Killen, R. M., M. Sarantos, A. E. Potter, and P. Reiff (2004), Source rates and ion recycling rates for Na and K in Mercury's atmosphere, *Icarus*, *171*, 1–19, doi:10.1016/j.icarus.2004.04.007.

Killen, R. M., T. A. Bida, and T. H. Morgan (2005), The calcium exosphere of Mercury, *Icarus*, *173*, 300–311, doi:10.1016/j.icarus.2004.08.022.

Killen, R. M., et al. (2007), Processes that promote and deplete the exosphere of Mercury, *Space Sci. Rev.*, *132*, 433–509, doi:10.1007/s11214-007-9232-0.

Killen, R., D. Shemansky, and N. Mouawad (2009), Expected emission from Mercury's exospheric species, and their ultraviolet-visible signatures, *Astrophys. J. Suppl.*, *181*, 351–359, doi:10.1088/0067-0049/181/2/351.

Killen, R. M., A. E. Potter, R. J. Vervack Jr., E. T. Bradley, W. E. McClintock, C. M. Anderson, and M. H. Burger (2010), Observations of metallic species in Mercury's exosphere, *Icarus*, *209*, 75–87, doi:10.1016/j.icarus.2010.02.018.

Leblanc, F., and R. E. Johnson (2010), Mercury exosphere I. Global circulation model of its sodium component, *Icarus*, *209*, 280–300, doi:10.1016/j.icarus.2010.04.020.

Madey, T. E., B. V. Yakshinskiy, V. N. Ageev, and R. E. Johnson (1998), Desorption of alkali atoms and ions from oxide surfaces: Relevance to origins of Na and K in atmospheres of Mercury and Moon, *J. Geophys. Res.*, *103*, 5873–5887.

McClintock, W. E., and M. R. Lankton (2007), The Mercury Atmospheric and Surface Composition Spectrometer for the MESSENGER mission, *Space Sci. Rev.*, *131*, 481–521.

McClintock, W. E., E. T. Bradley, R. J. Vervack, R. M. Killen, A. L. Sprague, N. R. Izenberg, and S. C. Solomon (2008), Mercury's exosphere: Observations during MESSENGER's first Mercury flyby, *Science*, *321*, 92–94, doi:10.1126/science.1159467.

McClintock, W. E., R. J. Vervack Jr., E. T. Bradley, R. M. Killen, N. Mouawad, A. L. Sprague, M. H. Burger, S. C. Solomon, and N. R. Izenberg (2009), MESSENGER observations of Mercury's exosphere: Detection of magnesium and distribution of constituents, *Science*, *324*, 610–613, 10.1126/science.1172525.

McGrath, M. A., R. E. Johnson, and L. J. Lanzerotti (1986), Sputtering of sodium on the planet Mercury, *Nature*, *323*, 694–696.

McLain, J. L., A. L. Sprague, G. A. Grieves, D. Schriver, P. Travinicek, and T. M. Orlando (2011), Electron-stimulated desorption of silicates: A potential source for ions in Mercury's space environment, *J. Geophys. Res.*, *116*, E03007, doi:10.1029/2010JE003714.

Mouawad, N., M. H. Burger, R. M. Killen, A. E. Potter, W. E. Mcclintock, R. J. Vervack Jr., E. T. Bradley, M. Benna, and S. Naidu (2011), Constraints on Mercury's Na exosphere: Combined MESSENGER and ground-based data, *Icarus*, *211*, 21–36, doi:10.1016/j.icarus.2010.10.019.

Mura, A., et al. (2009), The sodium exosphere of Mercury: Comparison between observations during Mercury's transit and model results, *Icarus*, *200*, 1–11, doi:10.1016/j.icarus.2008.11.014.

Nittler, L. R., et al. (2011), The major-element composition of Mercury's surface from MESSENGER X-ray spectrometry, *Science*, *333*, 1847–1850, doi:10.1126/science.1211567.

Potter, A. E. (1995), Chemical sputtering could produce sodium vapor and ice on Mercury, *Geophys. Res. Lett.*, *22*, 3289–3292.

Potter, A. E., and T. H. Morgan (1985), Discovery of sodium in the atmosphere of Mercury, *Science*, *229*, 651–653.

Potter, A. E., and T. H. Morgan (1986), Potassium in the atmosphere of Mercury, *Icarus*, *67*, 336–340.

Potter, A. E., and T. H. Morgan (1990), Evidence for magnetospheric effects on the sodium atmosphere of Mercury, *Science*, *248*, 835–838.

Potter, A. E., R. M. Killen, and M. Sarantos (2006), Spatial distribution of sodium on Mercury, *Icarus*, *181*, 1–12, doi:10.1016/j.icarus.2005.10.026.

Sarantos, M., R. M. Killen, A. S. Sharma, and J. A. Slavin (2010), Sources of sodium in the lunar exosphere: Modeling using ground-based observations of sodium emission and spacecraft data of the plasma, *Icarus*, *205*, 364–374, doi:10.1016/j.icarus.2009.07.039.

Sarantos, M., R. M. Killen, W. E. Mcclintock, E. T. Bradley, R. J. Vervack Jr., M. Benna, and J. A. Slavin (2011), Limits to Mercury's magnesium exosphere from MESSENGER second flyby observations, *Planet. Space Sci.*, *59*, 1992–2003, doi:10.1016/j.pss.2011.05.002.

Schleicher, H., G. Wiedemann, H. Wöhl, T. Berkefeld, and D. Soltau (2004), Detection of neutral sodium above Mercury during the transit on 2003 May 7, *Astron. Astrophys.*, *425*, 1119–1124, doi:10.1051/0004-6361:20040477.

Schriver, D., et al. (2011), Electron transport and precipitation at Mercury during the MESSENGER flybys: Implications for electron-stimulated desorption, *Planet. Space Sci.*, *59*, 2026–2036, doi:10.1016/j.pss.2011.03.008.

Slavin, J. A., et al. (2010), MESSENGER observations of extreme loading and unloading of Mercury's magnetic tail, *Science*, *329*, 655–668, doi:10.1126/science.1188067.

Slavin, J. A., et al. (2012), MESSENGER and Mariner 10 flyby observations of magnetotail structure and dynamics at Mercury, *J. Geophys. Res.*, *117*, A01215, doi:10.1029/2011JA016900.

Sprague, A. L. (1997), Mercury's atmospheric bright sports and potassium variations: A possible cause, *J. Geophys. Res.*, *97*, 18,257–18,264.

Sprague, A. L., et al. (1997), Distribution and abundance of sodium in Mercury's atmosphere, 1985–1988, *Icarus*, *129*, 506–527.

Vervack, R. J., Jr., W. E. McClintock, R. M. Killen, A. L. Sprague, B. J. Anderson, M. H. Burger, E. T. Bradley, N. Mouawad, S. C. Solomon, and N. R. Izenberg (2010), Mercury's complex exosphere: Results from MESSENGER's third flyby, *Science*, *329*, 672–675, doi:10.1126/science.1188572.

Vervack, R. J., Jr., W. E. McClintock, R. M. Killen, A. L. Sprague, M. H. Burger, A. W. Merkel, and M. Saratos (2011), Early MESSENGER results for less abundant or weakly emitting species in Mercury's exosphere, paper presented at EPSC-DPS Joint Meeting, EPSC, Nantes, France.

Weider, S. Z., L. R. Nittler, R. D. Starr, P. K. Byrne, D. K. Hamara, T. J. McCoy, and S. C. Solomon (2012), Compositional heterogeneity on Mercury's surface revealed by MESSENGER's X-Ray Spectrometer, *Lunar Planet Sci.*, *XLIII*, Abstract 1472.